Dynamics of Piton de la Fournaise volcano observed by passive image interferometry with multiple references

Christoph Sens-Schönfelder, Eraldo Pomponi, Aline Peltier

Journal of Volcanology and Geothermal Research 276 (2014) 32–45

Contents lists available at ScienceDirect

Journal of Volcanology and Geothermal Research

journal homepage: www.elsevier.com/locate/jvolgeores

Dynamics of Piton de la Fournaise volcano observed by passive image interferometry with multiple references

Christoph Sens-Schönfelder [a,*], Eraldo Pomponi [b], Aline Peltier [c]

[a] GFZ German Research Centre for Geosciences, Section 2.4, Potsdam, Germany
[b] University of Leipzig, Institute for Geophysics and Geology, Leipzig, Germany
[c] OVPF, Institut de Physique du Globe de Paris, Sorbonne Paris Cité, UMR 7154 CNRS, La Plaine des Cafres, La Réunion, France

ARTICLE INFO

Article history:
Received 20 November 2013
Accepted 12 February 2014
Available online 28 February 2014

Keywords:
Piton de la Fournaise
Volcano seismology
Volcano monitoring
Seismic interferometry
Precursory velocity changes
Deformation

ABSTRACT

Activity of Piton de la Fournaise (PdF) volcano in La Réunion Island modifies the seismic velocities within the edifice. Using the 2010 and 2011 data from a network of 21 seismic stations in the vicinity of PdF, changes of seismic velocities are investigated using passive image interferometry, i.e. interferometry of seismic noise correlations. As noise correlations change significantly over time in response to volcanic activity, a method is presented that allows us to measure continuous long term velocity changes with high and constant accuracy by using multiple periods as reference. A long term velocity increase is found that averages about 0.25% per year. This trend is superimposed by short term changes that exhibit a clear connection with summit seismo-tectonic earthquakes indicating the effect of volcanic activity. Characteristic signatures of velocity changes are identified for post-eruptive periods of deflation that show an increase of velocity associated with subsidence observed by GPS. Periods of pre-eruptive inflation are characterized by decreasing velocity. Seismic crises can be associated with either increasing or decreasing velocity depending on whether the magma movement leads to deflation due to an eruption emptying the shallow plumbing system or to inflation caused by a non-eruptive intrusion. With a simple assumption about the spatial sensitivity of the measurements both processes are found to have the strongest effect in the central summit area of the volcano which also shows the strongest surface displacements during the time investigated here. We do not observe a dependence of the velocity change on the location of the erupting fissures, instead the distribution of changes for the three inflation periods and the two eruptions are similar indicating that the velocity changes observed here reflect the dynamics of a shallow magma reservoir rather than the effect of the eruption at the surface.

1. Introduction

Seismic methods have successfully been used to investigate the internal structure of volcanoes with active sources (Aoki et al., 2009), earthquakes (Dawson et al., 1999; Berger et al., 2011), and ambient seismic noise (Brenguier et al., 2007; Nagaoka et al., 2012). Such investigations form the basis for earthquake locations by providing velocity models and they help in understanding the structural setting of magma transport. They also provide evidence for temperature anomalies and the presence of magmatic or hydrothermal fluids. But these properties are not constant. During phases of volcanic activity magma is transported along zones of structural weakness and pressure changes in the plumbing system cause deformation of the edifice. Though such processes are most likely to affect the velocity structure of the volcano, seismic observations of the dynamics are restricted to the study of seismic sources such as locations and source mechanisms of earthquakes and volcanic tremor. Tomographic investigations usually require periods of data acquisition that are longer than the time scale of the processes of interest and often do not provide sufficient accuracy to image weak changes. Only a few examples of 4D seismic tomography provide time resolved images of subsurface structure (Patanè et al., 2006; Calò et al., 2011).

The precision of velocity change measurements can be increased significantly by using scattered coda waves that propagate on intricate paths for a long time in the target medium and thereby accumulate the effect of medium changes such as time shifts caused by changes of the propagation velocity. Poupinet et al. (1984) demonstrated that the seismic coda excited by earthquake doublets can be used to measure velocity changes to a precision between 0.1% and 0.01%. The technique was extended under the term Coda Wave Interferometry by Snieder et al. (2002) and Snieder (2006) to include waveform changes as an additional observable to phase shifts.

With the possibility to monitor changes of velocity, seismic waves can be used to investigate the dynamics of volcanic processes directly. Continuous monitoring with high temporal sampling became possible with the development of seismic interferometry (e.g. Curtis et al.,

* Corresponding author.
E-mail address: sens-schoenfelder@gfz-potsdam.de (C. Sens-Schönfelder).

http://dx.doi.org/10.1016/j.jvolgeores.2014.02.012
0377-0273

2006; Larose et al., 2006; Wapenaar et al., 2010). The basic concept of seismic interferometry allows the record of a virtual seismic source located at *A* to be reconstructed at any position *B* in the medium by cross-correlation of a random wave field sensed at the two locations. As the ambient seismic noise, generated by atmospheric disturbances and ocean activity, has suitable characteristics for seismic interferometry the continuous measurements of ambient vibrations suffice to reconstruct signals from virtual sources. In contrast to earthquakes and active sources the signals from virtual sources can be repeatedly constructed from noise records at any time and allow direct comparison of waveforms from different time periods. The integration of seismic interferometry and coda wave interferometry was first presented by Sens-Schönfelder and Wegler (2006) at Merapi volcano as passive image interferometry (PII). Later this approach was used to study co-seismic variations in fault zones (Brenguier et al., 2008a; Wegler et al., 2009; Chen et al., 2010; Sens-Schönfelder and Wegler, 2011), co-eruptive changes at volcanoes (Brenguier et al., 2008b; Duputel et al., 2009; Mordret et al., 2010), seasonal changes (Meier et al., 2010; Hobiger et al., 2012; Richter et al., submitted for publication) temperature related velocity changes on the Moon (Sens-Schönfelder and Larose, 2008) and also clock errors of seismic stations (Sens-Schönfelder, 2008).

The volcano that was most intensively studied with PII is Piton de la Fournaise (PdF) on La Réunion Island (France) in the Indian Ocean (Fig. 1). There Brenguier et al. (2008b) observed for the first time seismic velocity changes associated with volcanic activity in the period from July 1999 to December 2000 using frequencies between 0.1 and 0.9 Hz. They consistently observe velocity reductions between 0.05% and 0.4% before eruptions that are superimposed on long term variations of unknown origin. Brenguier et al. (2011) also report waveform changes at high frequencies (0.5–3 Hz) associated with eruptions and velocity decreases not associated with eruptions. The authors speculate that the latter observation is related to intrusions that do not develop into an eruption. Duputel et al. (2009) analyze PdF data from 13 months following May 2006 that cover three eruptions. They confirm the observations of pre-eruptive velocity reductions and apply a regionalization technique and find that most intensive velocity variations are concentrated in the summit area of PdF. The observation of velocity increase during a period of deflation is interpreted as an effect of surface deformation by Duputel et al. (2009).

In this study we investigate data of a densified seismic network from September 2009 to December 2011. These 28 months of continuous data contain five eruptions, four seismic crises accompanied by deformation due to non-eruptive intrusions and four seismic crises without detectable deformation. Dates of these events are summarized in Table 1. This long period with diverse activity monitored by a dense seismic network provides new insight into the signature of velocity changes associated with different volcanic processes.

The article is organized as follows: Details about the investigated data are given in Section 2 and the description of the interferometric data processing in Section 3. In Section 4, temporal changes are investigated and a novel approach is presented; it uses multiple reference periods to stabilize the measurements in the presence of significant material changes. The spatial distribution of velocity changes is studied in Sections 5 and 6 and discussed in Section 7. Conclusions are summarized in Section 8.

2. Data

To investigate temporal changes of seismic velocities inside Piton de la Fournaise volcano we use seismic noise recorded by the permanent observatory network and the seismic stations that were installed during the UnderVolc experiment (Brenguier et al., 2012) run by the Institut de Physique du Globe de Paris, Observatoire Volcanologique du Piton de la Fournaise (IPGP/OVPF), and the Institut des Sciences de la Terre (ISTerre). In total 21 stations distributed in an area of about 10 by 16 km provide data for this study. The network is illustrated in Fig. 1. The map also shows locations of UnderVolc and OVPF GPS stations used to estimate surface displacements. GPS signals are recorded at a rate of 2 samples/min. Daily solutions are calculated using the GAMIT/GLOBK software. GPS trends of stations located on the terminal cone show edifice inflation/deflation directly linked to volcano activity, whereas GPS on the eastern flank show a continuous sliding of a few cm/yr to the east (Peltier et al., 2009; Brenguier et al., 2012; Clarke et al., 2013; Staudacher and Peltier, submitted for publication).

The number of seismic events per day was provided by the OVPF and is incorporated in this study as an indicator of volcanic activity. To assess the hydrological influence on the seismic velocity changes

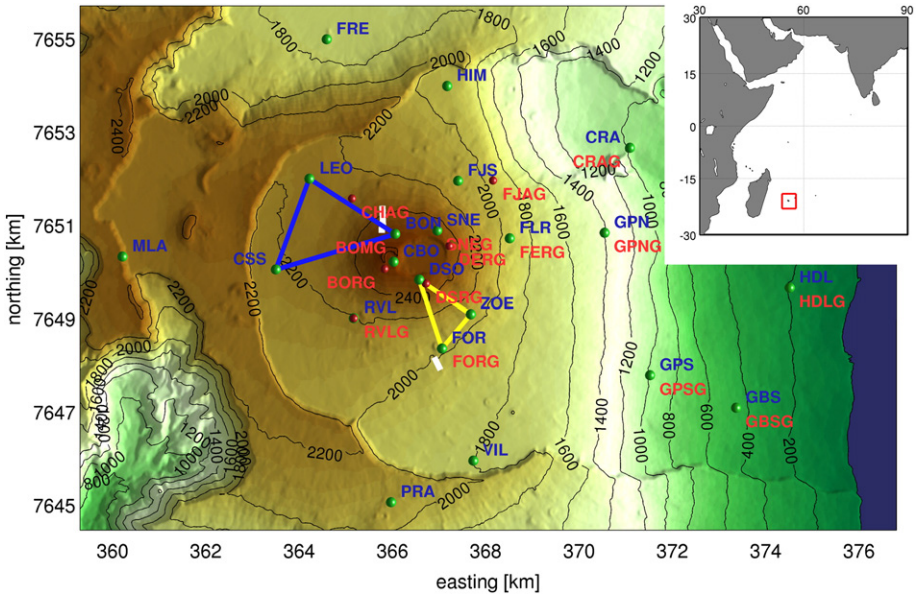

Fig. 1. Map of Piton de la Fournaise (La Réunion Island). Inset shows the location of La Réunion in the Indian Ocean. Indicated in green with blue labels are the seismic stations. Positions of GPS stations are shown in red. The eruption fissures of the two eruptions that occurred in late 2010 are indicated by white lines. Yellow and blue triangles connect the stations pairs for which velocity changes are shown in Fig. 5.

Table 1
Volcanic activity of Piton de la Fournaise during the study period as summarized by Roult et al. (2012). The intrusion labeled with * is identified here.

Type of event	Date
Eruptions	2009-11-05
	2009-12-14
	2010-01-02
	2010-10-14
	2010-12-09
Intrusions	2009-10-07
	2009-10-18
	2010-09-23
	2011-02-02*
Seismic crises	2009-10-14
	2009-10-30
	2009-12-29
	2010-09-19

we use data from a satellite and ground based global precipitation model (Huffman et al., 2001).

3. Seismic interferometry

As the first step of data analysis we apply seismic correlation interferometry to retrieve noise correlation functions (NCFs) from the seismic noise records. For ideal properties of the seismic noise field and long time averaging the NCFs would converge towards the Green's function. The continuous noise traces are cut into one hour long segments for time and frequency domain preprocessing. This step involves downsampling to 10 Hz sampling frequency, removal of the mean, spectral whitening, filtering in the 0.1 Hz to 4 Hz band and sign-bit normalization (Bensen et al., 2007). Cross-correlations of these one-hour segments are stacked in groups of 24 to obtain NCFs that are representative of individual days.

An impression of the NCFs is given in Fig. 2 which displays the correlations of the vertical components of all station pairs sorted according to the inter-station distance. Orientation of the NCFs is chosen such that noise propagating with a bearing of 290° ± 90° is displayed in the causal part at positive lag time. This direction best accounts for the asymmetry of the NCFs. It consistently causes larger amplitudes of the NCFs in the causal part and smaller amplitudes in the anti-causal part. This indicates that noise sources are predominantly located east–southeast of PdF. As expected for wave propagation in the heterogeneous medium the NCFs contain a direct wave propagating with about 1.3 km/s and strong coda waves excited by scattering.

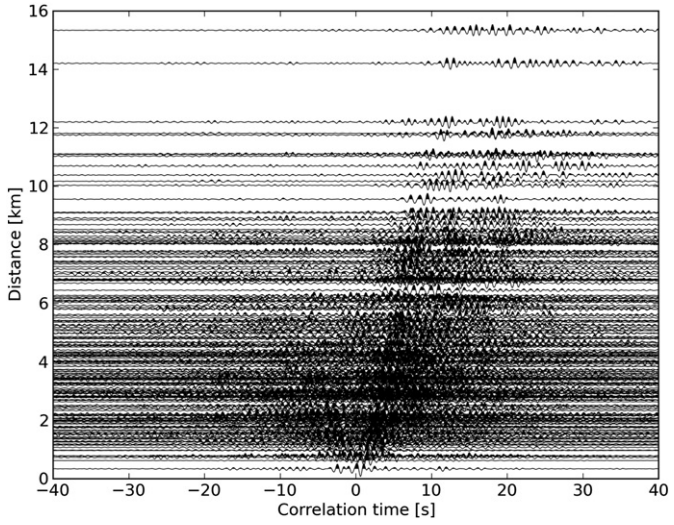

Fig. 2. Averaged correlation functions of the vertical components, filtered between 0.8 Hz and 1.5 Hz and ordered by inter-station distance.

4. Temporal variations of seismic velocity

Applying coda wave interferometry (Snieder et al., 2002) to the NCFs obtained in the previous section we investigated temporal changes of the propagation medium. We restrict here to changes of the propagation velocities. To quantify the velocity changes we apply the stretching method of Sens-Schönfelder and Wegler (2006), which compares short term NCFs to stretched or compressed versions of a reference NCF that is usually constructed by averaging all the available short term NCFs. For each daily NCF the correlation coefficient

$$C(\epsilon,t)=\frac{\int_{\tau_1}^{\tau_2}\phi(t,\tau)\phi_{ref}(\tau(1-\epsilon))d\tau}{\left(\int_{\tau_1}^{\tau_2}\phi^2(t,\tau)d\tau\int_{\tau_1}^{\tau_2}\phi^2_{ref}(\tau(1-\epsilon))d\tau\right)^{1/2}} \quad (1)$$

between the stretched reference and the daily NCFs is evaluated for a range of ϵ to obtain $\epsilon_{max}(t)=\mathrm{argmax}_\epsilon C(\epsilon,t)$ and $C_{max}(t)=C(\epsilon_{max}(t),t)$. $\epsilon_{max}=\mathrm{d}\,v/v$ is the apparent relative velocity change observed in the data that we denote Δv_a if it is required to distinguish the apparent value from true material change in the medium. C_{max} can be used as a measure for the uncertainty of ϵ_{max} (Weaver et al., 2011).

It has been shown in numerous applications to field data and laboratory test, that the stretching technique is very stable against noisy NCFs (Hadziioannou et al., 2009) and that fractional velocity changes below 0.1% can be measured in field data (e.g. Hobiger et al., 2012).

In initial tests we analyzed different frequency bands ranging from 0.05 to 4 Hz and chose the frequency band between 0.8 and 1.5 Hz as this showed the highest sensitivity to volcanic activity. Under the assumption of surface wave coda this frequency range provides sensitivity to a depth up to about 500 m. Additionally, the mode conversion to body waves provides sensitivity to greater depth (Obermann et al., 2013).

The lapse time window is set between 8 and 30 s based on the observed signal to noise ratio. We observe that the volcanic activity causes velocity changes that exceed 1% for some station pairs. Considering the combination of lapse time, frequency and amplitude of velocity variations it is clear that the resulting phase shift is not small compared to the dominant period. Consequently stacking of daily NCFs from the whole study period for the construction of the reference combines traces with a significant phase shift and leads to cancelation of late phases in the reference trace. On the other hand using only a short period of time for averaging will not fully utilize the potential for convergence towards the Green's function. To avoid alteration of the reference when NCFs with significant phase shift are averaged Richter et al. (submitted for publication) suggest the construction of the reference in an iterative process. In a first step an initial estimate of the velocity change is obtained with a preliminary reference constructed by the usual long term averaging. In a second step the NCFs are corrected for this initial estimate by appropriate stretching to construct a final reference by averaging the corrected NCFs. Such a reference does not suffer from phase shifts and is used to obtain the final estimate of $\mathrm{d}v/v$.

Here we propose another approach that is also suitable when the effects of the medium changes on the NCFs cannot be corrected by simple stretching. This is the case, for example, if the change in the medium is a strong local change instead of a small variation in an extended area. Such changes have been studied by Larose et al. (2010)) and Planès et al. (2014). An illustration of this effect is shown in Fig. 3 for different references. These figures illustrate the results of the stretching procedure for the station pair DSO–GBS with different choices of the reference period. The top panels of these figures show the normalized similarity matrices ($C(\epsilon,t)/C_{max}(t)$) that represent the correlation between the

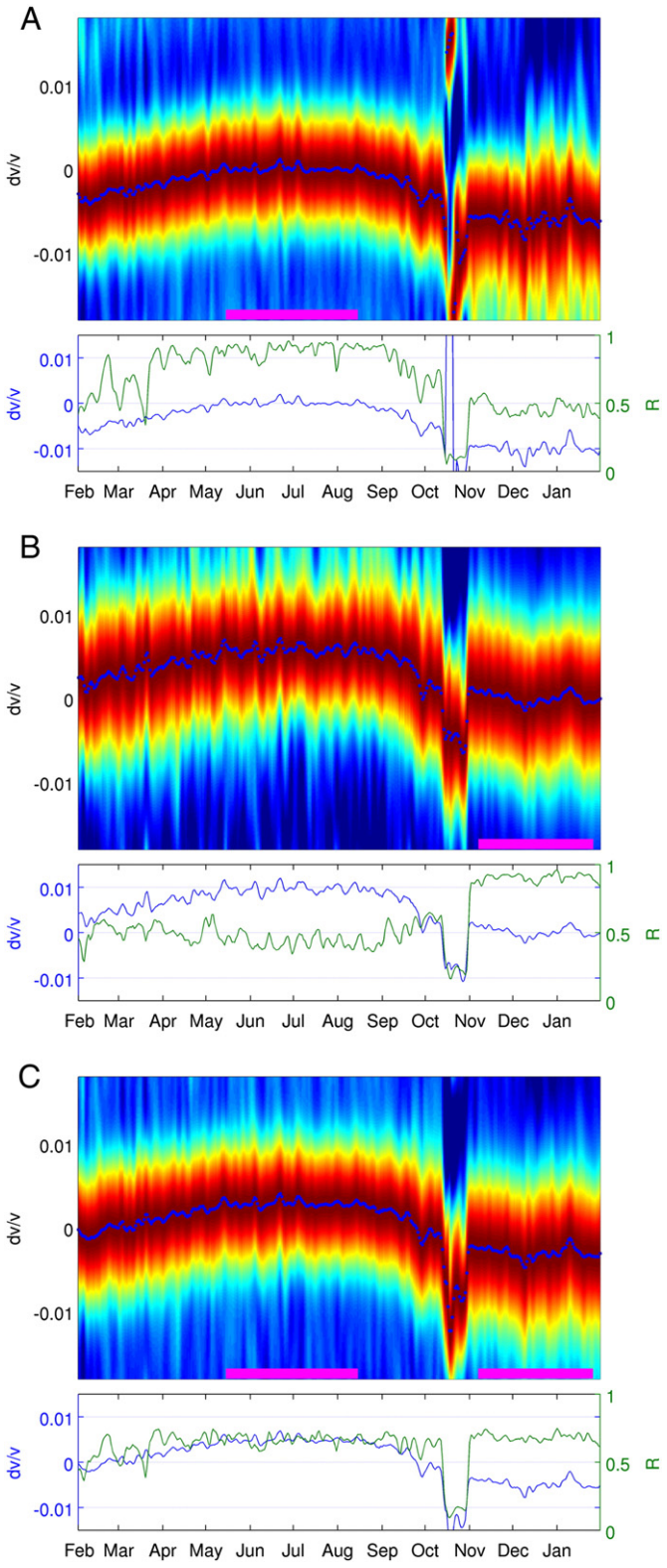

Fig. 3. Results of the stretching for station pair DSO–SNE in 2010 using different references. See text for detailed description. A: Reference obtained by stacking NCFs from May 15 to August 15. B: Reference obtained by stacking NCFs from November 10 to January 20. C: Combined references from A and B.

daily NCFs and the stretched references as a function of the stretching ϵ and time t. The bottom graphs show the curves of $C_{max}(t)$ and $\epsilon_{max}(t)$ in green and blue, respectively. Fig. 3A shows the measurement with a reference that is obtained by averaging daily NCFs from three months in the middle of 2010 as indicated by the purple bar. The correlation value shown in the bottom panel is close to one in the vicinity of the reference period but strongly decreases in October as the October 14 eruption introduced rather strong structural changes in the medium. The decreased correlation directly affects the precision of measurements in the period after November where the velocity changes show stronger fluctuations than before the eruption.

Similarly the reference can be constructed from the daily correlations of the time following the eruption as shown in Fig. 3B. Here we observe very good correlation and small fluctuations after the October eruption and strong fluctuations corresponding to small correlation before the eruption. This shows that the eruption introduced changes in the medium that degenerate the measurements if an unsuitable reference period is used. Mixing the two reference periods by averaging the references used in Fig. 3A and B does not improve the results as in this case the reference is neither similar to the period before nor after the eruption. Instead we propose to combine the two estimates from Fig. 3A and B by averaging the similarity matrices. Before averaging, the offset between the similarity matrices has to be corrected to place the ridges that represent optimal stretching on top of each other. This correction is done by shifting one of the matrices by the mean difference of the obtained velocity changes. The resulting averaged similarity matrix is displayed in Fig. 3C. It shows small fluctuations both before and after the October eruption and constant correlation value.

This approach is not limited to the use of two reference periods. In fact each of the N daily NCFs can be used as reference which would, however, result in a high computational effort as the stretching has to be performed N times. But it is possible to find compromise between a few measurements with well averaged and many measurements with weakly averaged reference correlation functions that is adopted to the dynamics of the investigated system. For the present dataset we perform the final measurements of velocity variations using monthly averaged references with an overlap of half a month resulting in 48 separate reference periods.

Using this approach we estimate the apparent velocity variations for all station pairs of the PdF network. To increase the significance of the measurements we performed the analysis for the three diagonal elements of the Green's tensor and averaged the estimated changes assuming that the coda wave field used here contains a mixture of wave types with similar sensitivities on all components.

The resulting apparent velocity changes for all station pairs are shown in Fig. 4 together with an average over all station combinations. A long term velocity increase can be observed that is sporadically

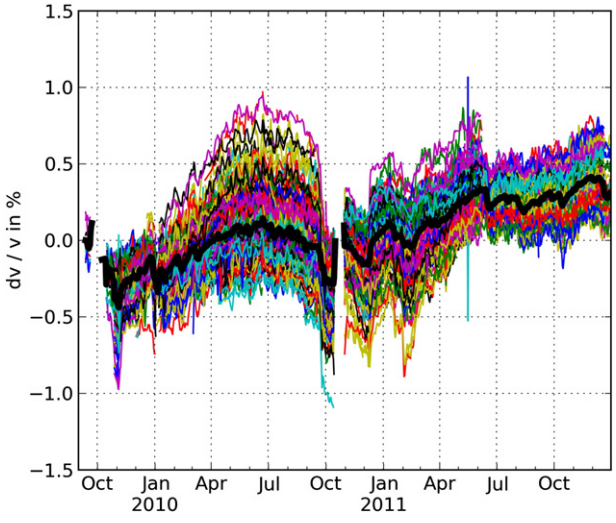

Fig. 4. Estimated velocity changes of all 210 station combinations of the PdF network. An average of the curves is indicated by a bold black line.

interrupted by abrupt changes. Short term erratic fluctuations allow us to assess the accuracy of the velocity change estimates that is below 0.1% for the measurements at single pairs. Though individual curves cannot be followed over the whole period in Fig. 4 it is clear that different station pairs show systematically different velocity changes.

5. Spatial variability of velocity changes

The temporal changes reported in the previous section show distinct patterns depending on the station pairs contributing to the correlation functions. To illustrate this, Fig. 5 shows the velocity changes observed at two groups of stations located to the south and to the north-west of the summit.

Clearly the long term variation from February to September has higher amplitude at the three station pairs south of the summit compared to the group in the north-west. Also the non-eruptive dyke intrusion at the end of September and the subsequent eruption cause distinct signals at the two groups. This different behavior between the two groups is a clear indication of spatially inhomogeneous velocity changes and their imprint on the NCFs that depends on the location of the stations.

Based on this observation we study the spatial distribution of the subsurface velocity variations obtained by inverting the *apparent* velocity changes observed as phase shifts in the cross-correlation functions between pairs of stations. This tomographic inversion requires knowledge about the spatial sensitivity of the measurements for local changes of velocities. Such sensitivity kernels for phase shifts were derived by Pacheco and Snieder (2005) under the assumption of diffuse wave propagation and for the case of single scattering by Pacheco and Snieder (2006). Larose et al. (2010), Rossetto et al. (2011) and Planès et al. (2014) investigated the sensitivity kernels for the decorrelation of the coda wave field in response to isolated impedance changes, i.e. localized defects. Both measures — phase shift and decorrelation — lead to similar forms of the kernel K for the sensitivity of diffuse waves:

$$K(\mathbf{x},\tau) = \frac{\int_0^{\tau} g(\mathbf{s},\mathbf{x},\tau-\tau')g(\mathbf{x},\mathbf{r},\tau')d\tau'}{g(\mathbf{s},\mathbf{r},\tau)} \tag{2}$$

where $g(\mathbf{s},\mathbf{r},\tau)$ is the intensity of a field excited at the location of the source $\mathbf{s}$ recorded at the receiver location $\mathbf{r}$ at time τ. The intensity $g(\mathbf{s},\mathbf{r},\tau)$ can be interpreted as the probability of a random walker that starts at $\mathbf{s}$ to be at $\mathbf{r}$ at time τ. In this interpretation $K(\mathbf{x},\tau)$ is the probability of the random walker that starts at $\mathbf{s}$ to visit location $\mathbf{x}$ before arriving at time τ at the location receiver $\mathbf{r}$. The apparent velocity change Δv_a that is observed in the data is related to the local changes $\frac{dv}{v}(\mathbf{x})$ measured in the NCFs by

$$\Delta v_a(\tau) = \frac{1}{\tau}\int_V K(\mathbf{x},\tau)\frac{dv}{v}(\mathbf{x})dV. \tag{3}$$

A cross section of the kernel through the receiver plane is shown in Fig. 6 for parameters in a representative range for the present investigation.

Although it was shown by Planès et al. (2014) using numerical wave field simulations that the general formula for K in Eq. (2) is a good approximation for a wide range of the mean free path, there are significant uncertainties about the precise shape of K. These originate from the generally poorly known scattering properties of the medium and the time and frequency dependent conversion between surface and body waves (Obermann et al., 2013).

Considering this uncertainty we follow the strategy proposed by Hobiger et al. (2012) to approximate the kernel K with the sum of two δ-functions peaked at the locations of the receivers:

$$K(\mathbf{x}) = \frac{1}{2}[\delta(\mathbf{x}-\mathbf{s}) + \delta(\mathbf{x}-\mathbf{r})] \tag{4}$$

where $\mathbf{s}$ and $\mathbf{r}$ are again the positions of source and receiver respectively or the positions of the two stations if NCFs are used. With this approximation, it follows that the apparent velocity change Δv_a observed at a pair of stations is simply the mean of the local changes at the two stations: $\Delta v_a(\mathbf{s},\mathbf{r}) = 1/2(\Delta v(\mathbf{s}) + \Delta v(\mathbf{r}))$. The sensitivity matrix G of the corresponding inversion problem:

$$\Delta \mathbf{v}_a = \mathbf{G}\Delta \mathbf{v} \tag{5}$$

is sparse with only two entries per row. It can easily be inverted in a least squares sense as the system is overdetermined for more than 3 stations.

Fig. 7A shows the curves that result from this inversion and represent the velocity changes in the surroundings of the stations. These curves show episodes of rapidly decreasing velocities and periods of smoothly varying velocities. Clearly the dynamics is different for different stations indicating that the velocity changes are spatially heterogeneous. To test whether the model with the delta-like sensitivity kernels is able to capture this heterogeneity we quantify the performance of our model with the F-test. For this we construct an optimized model of homogeneous velocity changes that has a single free parameter ($P_1 = 1$). As temporal evolution of the homogeneous velocity change we use the mean of all measurements as indicated in Fig. 4. The optimization of this model involves a constant that is added to the measurements from each station pair to minimize its offset from the mean change.

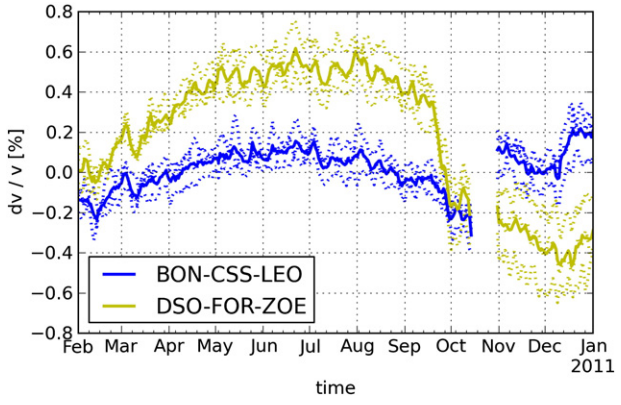

Fig. 5. Observed apparent velocity changes of a data subset for two station groups in the north-west (blue curves) and the south of the summit (yellow curves) as indicated by the triangles in Fig. 1. Curves for individual pairs are dashed and averages within the two groups are shown with bold lines.

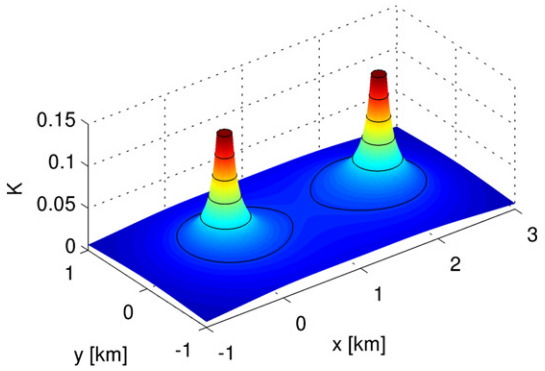

Fig. 6. Spatial sensitivity at 20 s lapse time for a station pair at distance of 2 km located at the poles of K. The transport mean free path is 1 km and the velocity is set to 1 km/s.

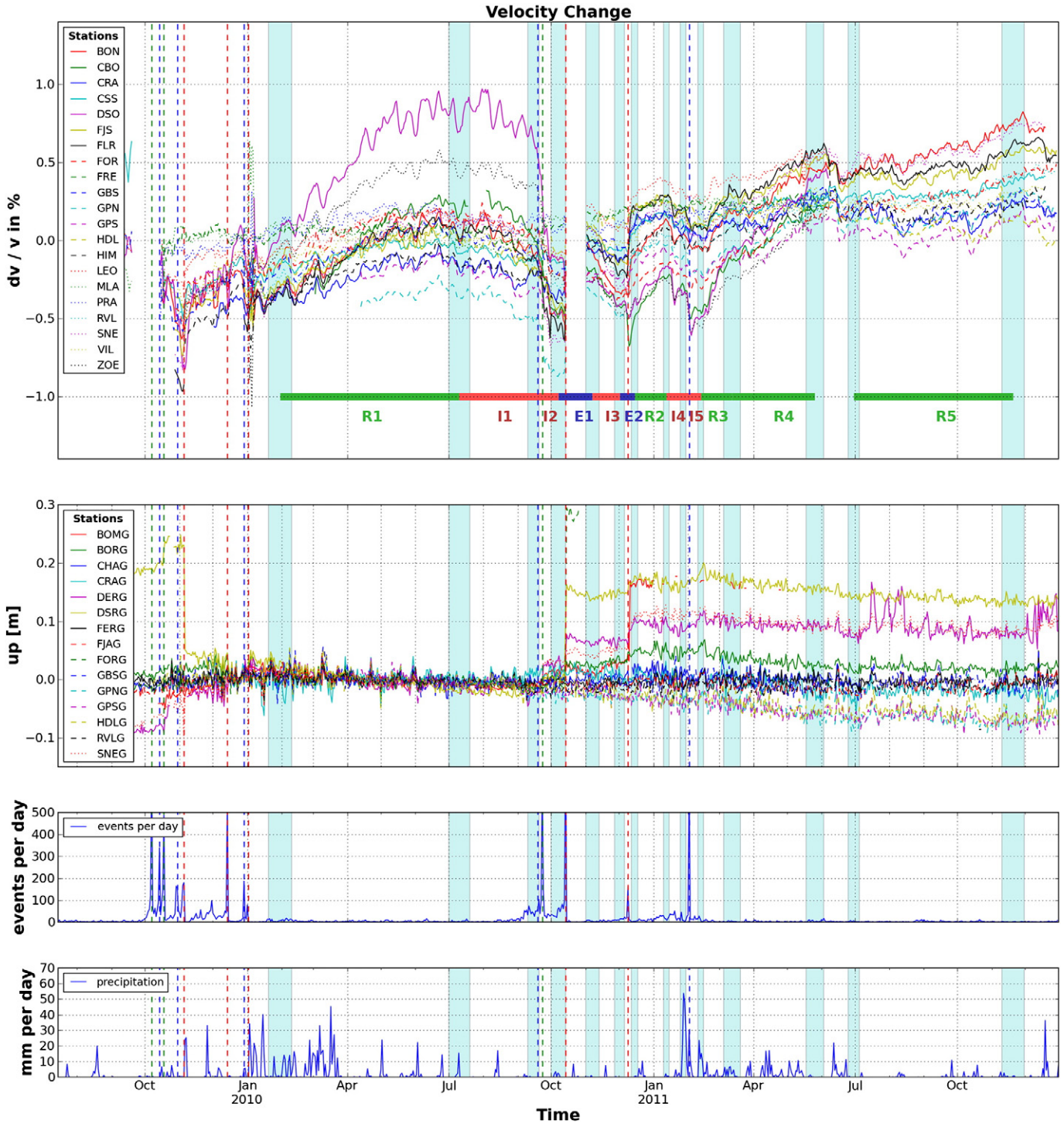

Fig. 7. Time series characterizing the dynamics of the volcano. A: Velocity variations at the locations of the seismic stations. B: Vertical displacements at GPS stations. C: Seismic activity at the summit as number of detected events per day. D: Precipitation obtained from satellite observations (Huffman et al., 2001). Vertical dashed lines indicate volcanic activity: seismic crisis (blue), seismic crisis with detectable deformation indicating a non-eruptive dyke intrusion (green), beginning of eruptions (red). Vertical light blue bars indicate the periods of stable velocities used for averaging. Horizontal lines show the intervals in which velocity changes are mapped.

The residuals of this model are compared with the residuals of the model with heterogeneous velocity changes that has $P_2 = 21$ (number of stations) degrees of freedom. We find that the simple way of assigning the different changes to the locations of the stations results in a significantly better description of the data for about 80% of the time. The remaining 20% in which our model is not significantly better than a model of homogeneous changes include periods in which the heterogeneous model also predicts homogeneous changes and data gaps during eruptions.

For the interpretation of these curves Fig. 7 shows vertical GPS displacements, seismic activity at the summit and daily precipitation in panels B, C, and D respectively. Common dynamics in these data is easily identified by means of the seismicity. Seismic activity exceeding more than 100 events/day is always reflected by abrupt displacements and velocity changes. This is the case for all eruptions indicated by vertical red dashed lines in Fig. 7. Intrusions identified by a seismic crisis with associated surface deformation are indicated

with dashed blue lines and similarly cause abrupt seismic velocity changes.

During inter-seismic periods displacement vectors generally show slow subsidence documenting a continuous relaxation of the edifice after the major crater collapse in 2007 (Peltier et al., 2010; Staudacher and Peltier, submitted for publication). These periods are generally accompanied by increasing velocities. Exceptions are the periods before the non-eruptive intrusion and subsequent eruption of September/October 2010 and before the eruption of December 2010 when velocity decreases despite a low level of seismic activity.

A clear relation with the precipitation cannot be established.

6. Imaging changes

In the previous section we obtained an approximation for the distribution of velocity changes in the subsurface from measurements of apparent changes at various station pairs. Though this results in estimates that are representative for the vicinity of the stations, we use this information for a spatial representation of the velocity changes by interpolating between stations with a nearest neighbor algorithm. Different choices for the interpolation scheme are possible but as we can only speculate about the character of the spatial velocity changes the nearest neighbor method is a conservative choice.

As the velocity changes exhibit complicated and spatially different temporal evolution it is not useful to chose a global reference for mapping changes relative to this reference. Instead we wish to map the distribution of velocity changes between two states of the volcano, i.e. we want to map the effects of isolated processes that change the elastic properties of the volcano in the respective time span. To identify changes related to such an isolated process we define periods that describe the state of the volcano before and after the action of the process. A number of such periods (blue shaded vertical stripes in Fig. 7) can be used to characterize the evolution of the system. Depending on the volcanic activity these periods are of different durations as specified in Table S1. Within these periods the velocity changes are averaged to reduce fluctuations. In the same way GPS position measurements are averaged within these periods and displacement vectors are obtained as difference between the averaged positions in the two states.

In the interest to separate the effects of different volcanic processes we require a certain temporal distance between events to obtain a stable measurement of the velocities before and after each event. This requirement is problematic for the investigation of the active sequence between October 2009 and January 2010. Activity in this sequence is rather strong with eight events (seismic crisis, intrusions and eruptions) in four months which makes it impossible to isolate individual processes. Additionally considering that the network was not yet complete in 2009 we decide to restrict the detailed analysis in the following sections to the years 2010 and 2011 in which seismic data are of superior quality and activity is sufficiently separated in time.

In the time intervals between the periods that indicate different states of the volcano, different processes are active and change the system. In Fig. 7 a number of such intervals is indicated by horizontal lines and named with the letters I, E, and R indicating inflation, eruption and relaxation respectively. Additional numbers distinguish active intervals of the same type. The identification of the processes that we assign to the different intervals is based on the observed pattern of velocity changes and supported by surface displacements and volcanological information. We show that intervals in which the dominant process can be unambiguously identified with volcanological information show distinct patterns of velocity changes. These patterns re-occur even when independent observation is not available or less clear and lead us to the assignment of the process to the intervals.

To illustrate how the surface displacements and velocity changes are related to the topography, the volcano is shown in perspective view in Fig. 8. Velocity changes for interval I2 that contains a well documented non-eruptive dyke intrusion on September 23 (Roult et al., 2012) are overlain in color and surface displacements are indicated by red and blue arrows. Red arrows for upward motion point away from the sensor location. For downward motion arrows are blue and point towards the sensor. Interval I2 shows a decrease of velocities up to 0.8% in the central part of the edifice around the main crater. This is also the region that experienced the most significant surface displacements. The central stations show a clear expansion pattern with upward and outward motions. Stations on the flanks show little movement on this time scale, corresponding to stable seismic velocities.

To facilitate the display for other intervals, results are shown in top view in Figs. 9, 10, and 11.

6.1. Intervals of edifice inflation

Interval I2 (Figs. 8 and 9A) as discussed above contains a non-eruptive dyke injection that was accompanied by a seismic crisis. It was detected by GPS data and a long period signal at a seismic broadband station located 8.5 km north of the summit (Roult et al., 2012). The displacement vectors in the summit area point in radial direction outward from the central crater with a strong upward component. This documents the expansion of the edifice caused by the magmatic intrusion. Velocities drop in the central part of the volcano. The interval

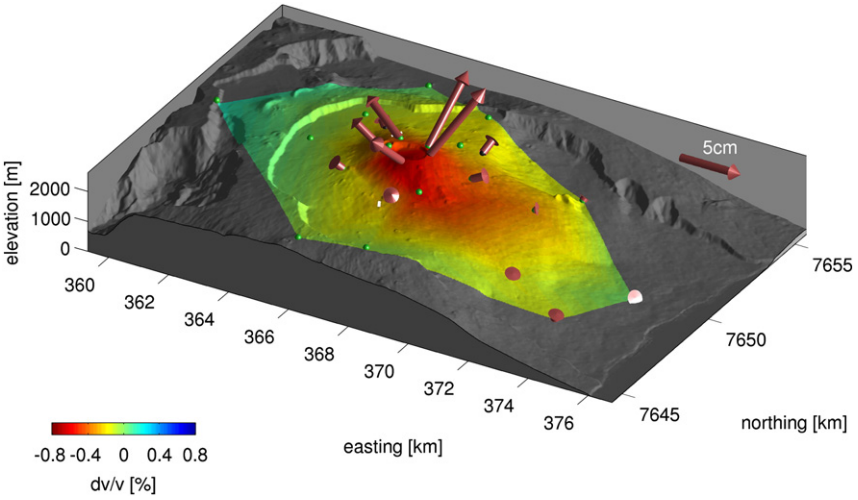

Fig. 8. Distribution of velocity changes for interval I2 (Fig. 7) in UTM coordinates zone 40 south. Displacements at GPS stations are indicated by arrows that are plotted blue and point towards the measurement location if motion is downward and plotted red pointing away from the station for uplift. Length scale for displacements is indicated at the northern edge of the plot. Horizontal and vertical scales of the elevation are identical.

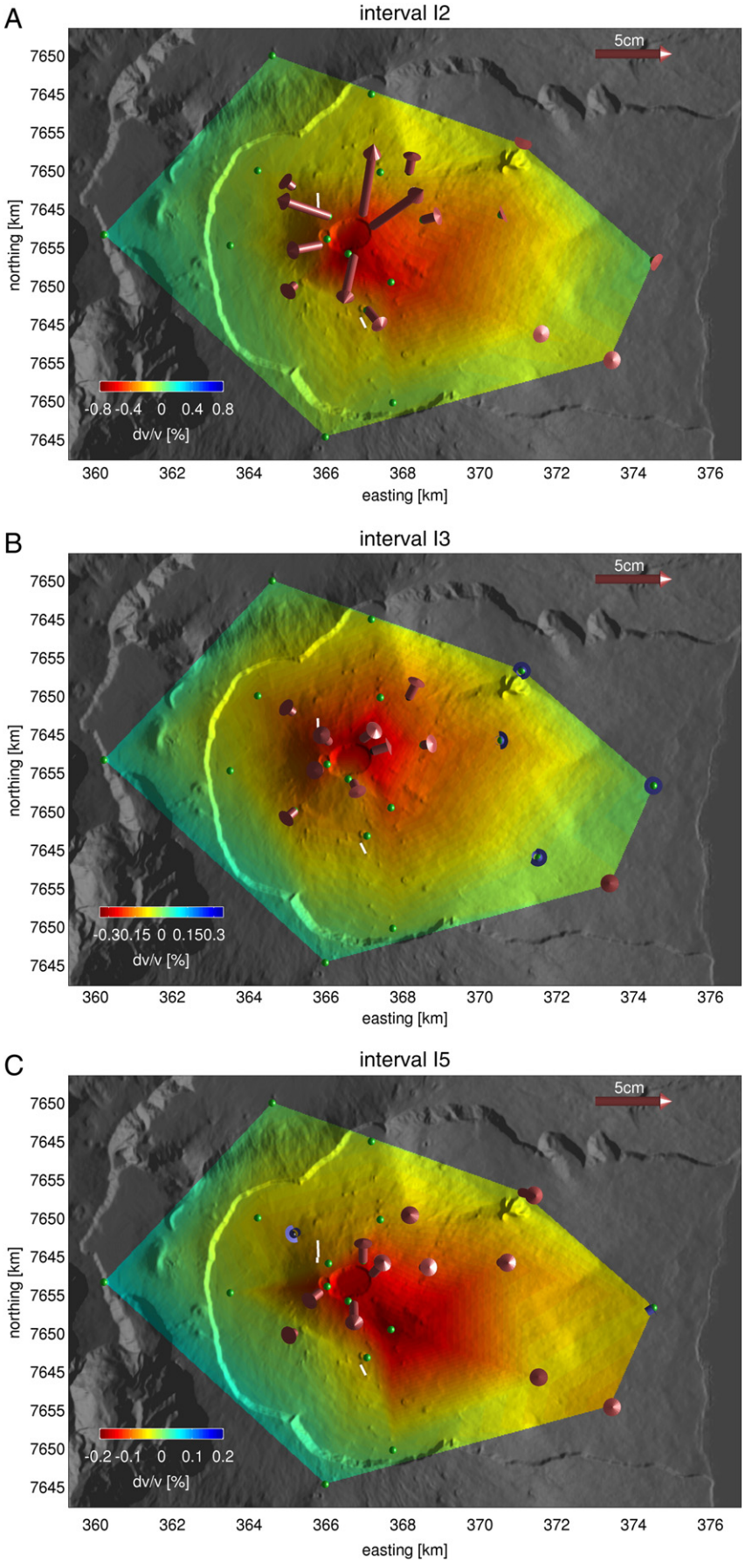

Fig. 9. Velocity changes associated with time intervals of inflation. Annotation of the time intervals referring to Fig. 7 is above the graphs.

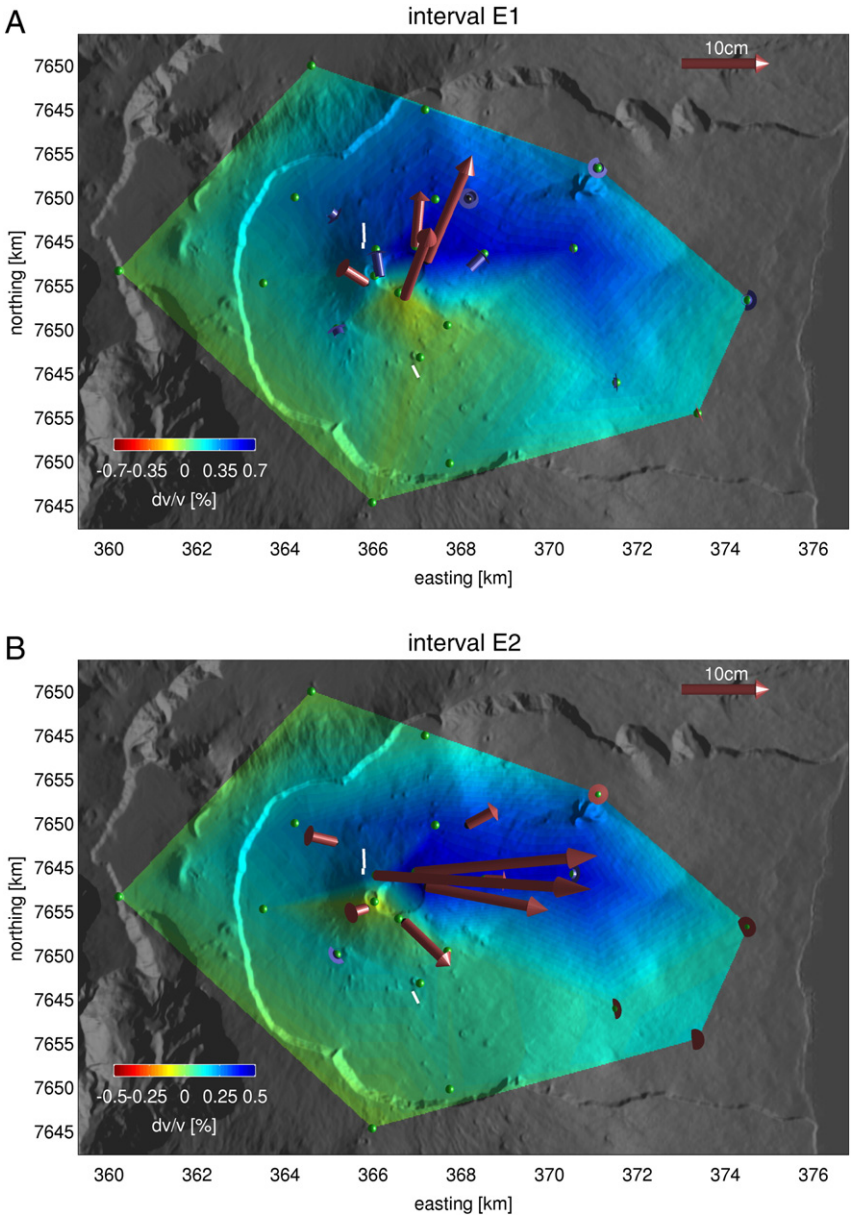

Fig. 10. Velocity changes associated with time of eruptions. Annotation of the time intervals referring to Fig. 7 is above the graphs.

directly precedes the eruption of October 14 on the southern flank. We use this interval (I2) as prototype to identify episodes of inflation.

The three most significant intervals of inflation (including I2) are shown in Fig. 9. Following the October 14 eruption, interval I3 shows velocity changes similar to I2 and is thus classified as affected by inflation (Fig. 9B). This is confirmed by surface displacements. Again central stations move up and outwards.

A third interval of decreasing velocities that we classify as inflation is I5 in January and February 2011 (Fig. 9C). This is a two phase episode starting with a weak abrupt velocity decrease in middle of January (I4). This change is not accompanied by a seismic crisis though the number of events is slightly elevated compared to quiet periods. The distribution of velocity changes in I4 is shown in Figure S1 (supplementary material). A second larger drop, that amplified the signal, occurred in I5 on February 1 coincident with a seismic crisis (Fig. 9C). The spatial pattern of changes in both phases is slightly different and changes from a large scale signal in the first phase to a more focused signal peaked south east of the crater in the second phase.

The distribution of changes in I1 is shown in Figure S2 of the supplement.

6.2. Eruptions

Velocity changes associated with the two eruptions that occurred in 2010 are displayed in Fig. 10. Both eruptions follow intervals identified as inflation in the previous section and are directly preceded by seismic crises of a few hour/minute duration. The first eruption in interval E1 followed the non-eruptive dyke intrusion of September and occurred on October 14 on the southern flank (Fig. 10A). Opposed to the symmetric pattern of the velocity decrease during inflation the eruption is accompanied by a velocity increase north of the crater. In the southern parts the velocity remains constant. The surface displacements also exhibit a heterogeneous pattern. Stations move to the north away from the eruptive fissure on the south flank with strongly variable amplitudes.

This pattern re-occurs in the interval that contains the December 9 eruption (Fig. 10B) that activated a fissure directly northwest of the crater. Again velocities increase in the northern half of the volcano while the stations in the south keep constant seismic velocities. Surface displacements are different from the October eruption but again with vectors pointing away from the active fissure.

6.3. Intervals of edifice relaxation/deflation

Intervals of seismic quiescence without volcanic activity do not correspond to periods of constant velocities. The prototype for such inactive periods is interval R1. It follows the intensive volcanic activity of 2009. Even though R1 does not contain any seismic activity and no abrupt deformation event we detect pronounced changes of seismic velocities. R1 shows a concentric pattern of increasing velocities centered around the summit and decaying with increasing distance. Surface displacements show a similar pattern of continuous concentric movements with vectors pointing down and inwards. This indicates deflation/relaxation with surface motion almost opposite to intervals of inflation (cf. Fig. 9A).

Other examples of intervals classified as affected by deflation/relaxation (R2, R3, and R4) are shown in Fig. 11B, C, and D. R2 (Fig. 11B) is the interval following the December 9 eruption. We observe decreasing velocities of smaller amplitudes as compared to R1 in the central area except to the northeast where velocities remain constant. Surface displacements in interval R2 are small with variable directions showing subsidence as well as uplift.

R3 is the interval that directly follows the period that we classify as inflation in early 2011. The pattern of the velocity change is similar to R1 and again surface displacements indicate deflation. In Interval R4 the rate of velocity change slows down as compared to R3 (cf. Fig. 7) but we still observe decreasing velocities with the pattern typical for periods of deflation. In interval R5 (supplementary Figure S3) the number of station decreased but we still observe increasing velocities.

7. Discussion

In the previous sections we showed that substantial changes of seismic velocities can be observed at the seismograph stations on Piton de la Fournaise. We observe long term variations as well as instantaneous changes that occur mostly coincident with rapid surface deformation and seismic events in the summit area.

7.1. Mechanism of velocity changes

The observed connection between surface displacements and seismic velocity changes raises the question for its physical mechanism.

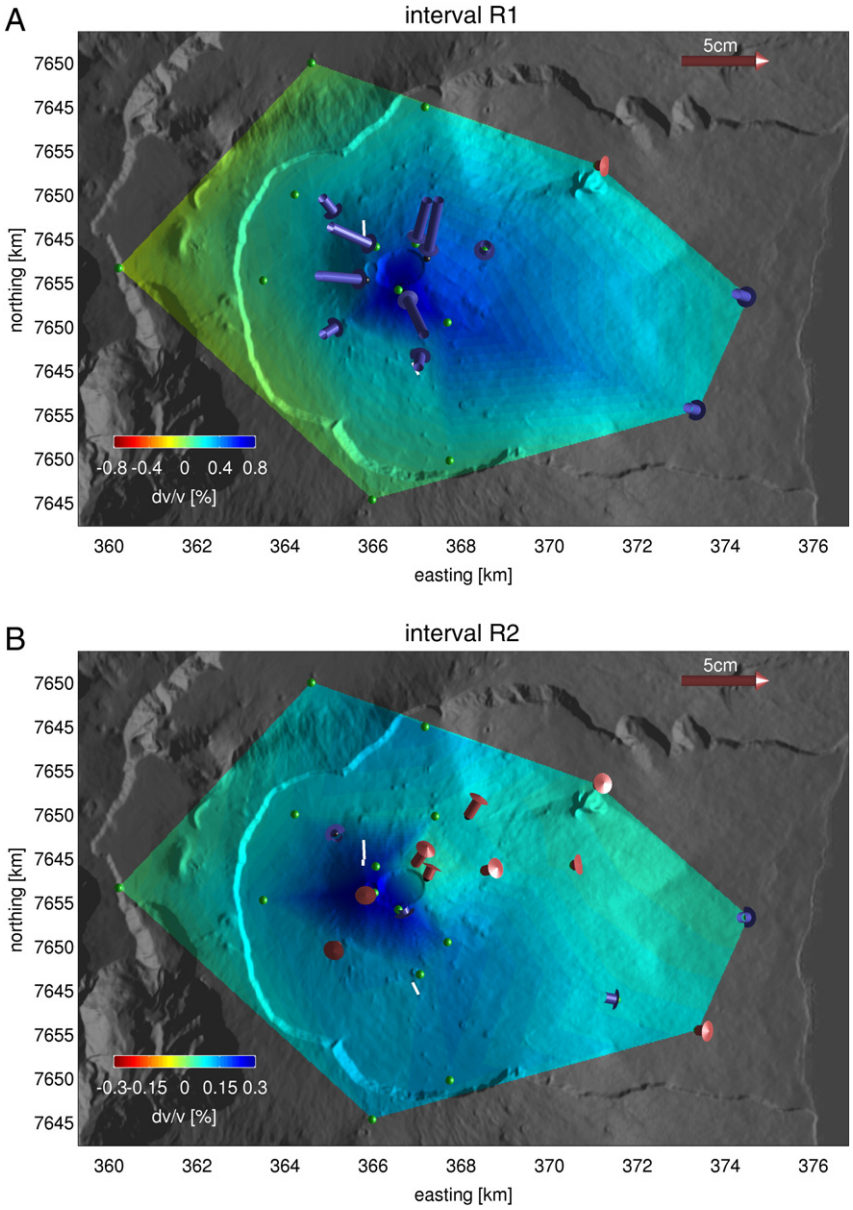

Fig. 11. Velocity changes of intervals classified as relaxation. Annotation of the time intervals referring to Fig. 7 is above the graphs.

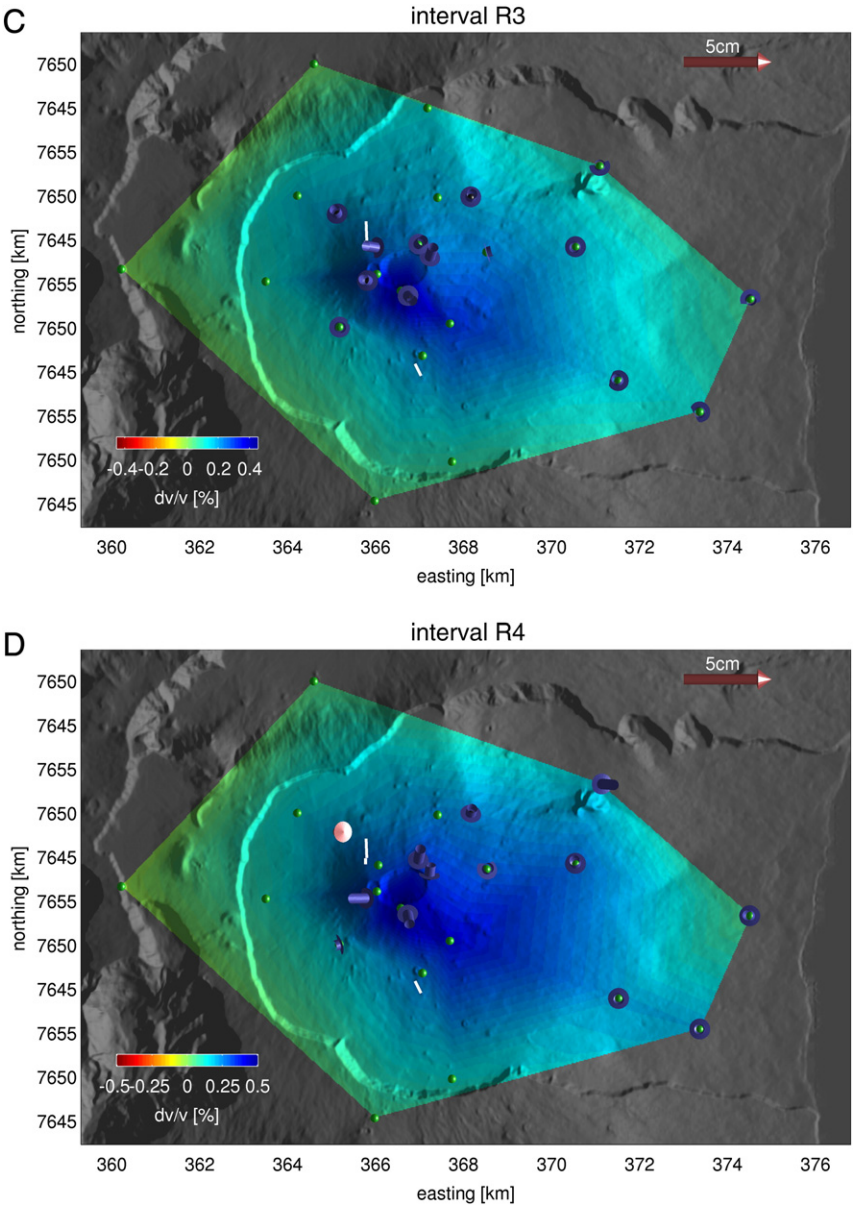

Fig. 11 (*continued*).

The most obvious first order effect is a time delay of seismic phases caused by increased (or decreased) distances between stations after inflation (or deflation). This effect can be ruled out as the relative distance change is about one order of magnitude smaller than the observed velocity change. As our measurements are based on seismic coda the distance effect is even smaller.

The second more realistic mechanism results from the stress sensitivity of seismic velocities (Toupin and Bernstein, 1961). A poro-elastic model for this mechanism is described by Shapiro (2003) using a differentiation of the pore space into stiff and compliant pores depending on their aspect ratio. Compliant porosity composed of thin cracks and the vicinity of grain contacts leads to a high stress sensitivity of velocities at low confining pressure close to the surface. At greater depth (higher confining pressure) compliant pores are closed and only the lower stress sensitivity of stiff porosity remains. This effect counteracts the need for a deep reaching depth sensitivity of the seismic measurements as stress related velocity changes are amplified in shallow layers. In relation to this mechanism we interpret the observed velocity changes as caused by changes in the confining pressure, i.e. the trace of the stress tensor. Due to the free surface effect a pressure increase at depth lowers the confining pressure at the surface. Got et al. (2013) investigate the deformation field of an eruption at PdF and model the stress changes induced by various sources of deformation. The extent of tensional stress changes in the model for a summit inflation well matches the extent of the velocity decrease observed here.

In case of significant pore pressure the relevant quantity is the differential pressure which, is the confining pressure reduced by the pore pressure. This means that an increase in pore pressure caused for example by the release of volatiles from injected magma would act similar to a decrease of confining pressure.

With this interpretation of the velocity changes we can re-evaluate our measurements in connection to the activity of PdF. The activity of PdF in the investigated period in 2010 contains two eruptions and one non-eruptive dyke intrusion confirmed in an independent investigation (I2, Roult et al., 2012). For these well documented episodes we observe the characteristic patterns of velocity changes as described in Section 6.

However, especially between these active episodes when there is no peculiar surface displacement or seismic activity the observations of seismic velocity changes can provide complementary information and contribute to the understanding of the volcano dynamics in these periods.

7.2. Non-eruptive dyke injection of September 2010

A specifically interesting example is the preparatory phase of the two eruptions in end of 2010. In contrast to the surface displacements that show sudden signals at the time of the dyke injection (September 23) and seismic activity that increases around September 10, the velocities already indicate a change of activity in August. From the time series in Fig. 7 it is clear that the period of increasing velocities indicating deflation ends in the middle of 2010 and the trend gradually reverses until September indicating inflation (interval I1 in Fig. 7). Though GPS data in this interval still indicates subsidence (until end of August) the spatial pattern of the velocity changes shown in Fig. 12 can already be classified as inflation. This period is also free of any significant precipitation that might have perturbed the velocities. In September the trend is strongly amplified when the increasing rate of seismicity and surface displacements documents the magma migration on September 23.

The observation of a velocity signal without detectable surface displacements indicates that surface deformation is not the only mechanism affecting the seismic velocities. Instead, due to deeper reaching sensitivity compared to GPS, the velocity changes in interval I1 might result from deformation at depth or magmatic fluids released from the pressurized reservoir.

7.2.1. Eruption of October 2010

The dyke injection on September 23 causes a significant velocity change of more than half a percent at the summit stations. After the magma injection, velocities remain almost constant until the onset of the eruption of October 14 when the volcanic tremor deteriorates the cross-correlation functions leading to the loss of information about velocity changes. After the eruption we obtain stable Green's functions again and can estimate the change that was introduced by the eruption. This eruption, located on the southern flank, caused a drastic increase of velocity but affected mostly stations in the northern half of the volcano. Stations in the south are much less affected and velocities remain almost constant. This appears surprising, as the fissure of the October eruption is located south of the crater. However, two processes are interacting during this interval. On the one hand movement of magma induces a local and shallow perturbation at the surface around the active fissures probably leading to a local decrease of velocity. On the other hand the deeper magma reservoir feeding the eruption is emptied causing a spatially extended increase of velocities. Assuming that the eruption returned the magma system to the state before the inflation period, we can image the permanent change caused by the eruption by mapping the change in an interval that contains both the inflation and the eruption (i.e. I2 and E1) as shown in Fig. 13. Clearly the permanent changes that remains from the intrusion after the eruption is a velocity decrease focused at two stations on the south-east flank uphill of the eruption fissure. The change introduced by the inflation period in the other parts of the volcano was reversible and vanished during the eruption.

Following this eruption we do not observe a relaxation signal. Instead another interval of inflation appears to prepare the eruption of December 2010.

7.2.2. Eruption of December 2010

Directly following the October 2010 eruption seismic velocities continue to decrease indicating another period of inflation (I3 in Fig. 9B). The decrease appears to be stronger in the northern part that did not experience permanent velocity decrease in September/October.

Though amplitudes are different, the distribution of velocity changes during the December eruption is remarkably similar to the October eruption. We do not observe a clear indication of the location of the eruption fissure (Fig. 10B). Also the similarity of the velocity changes in the inflation phases preceding the two eruptions suggests a common feeding system.

Such a sequence of eruptions during an eruptive cycle is common at PdF (Peltier et al., 2009). Eruptions can affect both the northern and southern flank of the volcano and originate from a common magma reservoir around sea level (about 2500 m below the summit). From the 1998 seismic swarm Battaglia et al. (2005) relocated seismicity that traces magma ascent to this reservoir and then follows the paths from this reservoir to the locations of the two subsequent eruptions. Massin et al. (2011) re-located seismicity associated with the 2007 eruptions and also identified a shallow magma reservoir around sea level as the common source.

Following the eruption in interval E2 relaxation is clearly identified by the increasing velocities in interval R2 (Fig. 11B) that lasts until middle of January 2011.

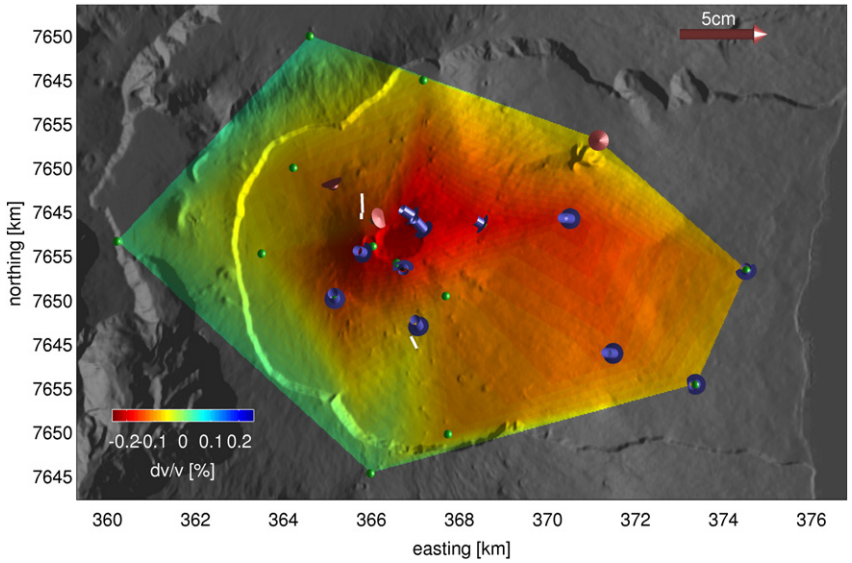

Fig. 12. Observed velocity change for period I1.

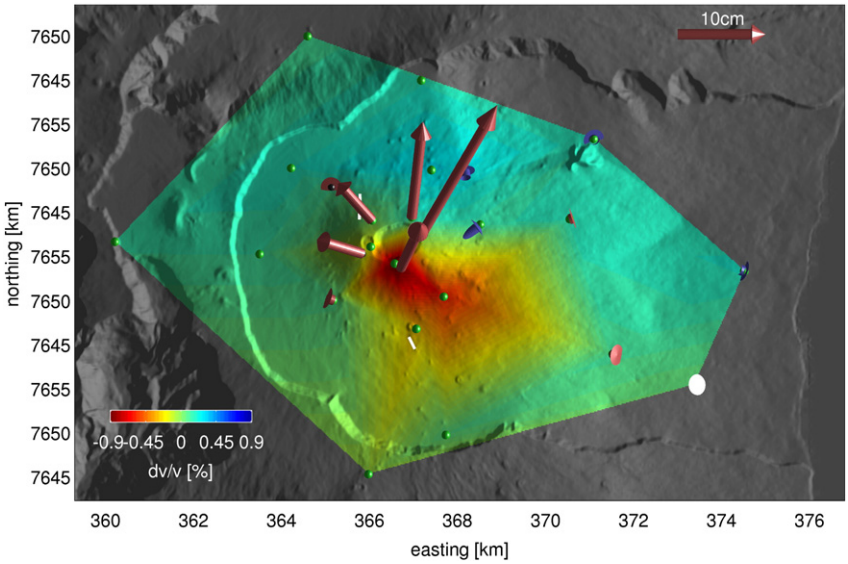

Fig. 13. Observed velocity change for period I2–E1.

7.2.3. Activity in 2011

The relaxation period after the December 2010 eruption is interrupted by a two step episode of decreasing velocities beginning in January 20, 2011. Whereas the first step was accompanied by only slightly increased seismic activity, the second step on February 2 occurred coincident with a seismic crisis. The spatial distribution of both phases clearly shows the pattern characteristic of inflation but affected mostly the southwest flank of the crater similar to the intrusion of September 2010. Seismic velocities remain almost stable until February 18 when they start to increase again showing a relaxation pattern. The two step character reminds of the non-eruptive intrusion September 23 (I2) that was also preceded by a weak inflation signal in I1.

From this date velocities increase continuously until the end of 2011. This trend is interrupted by a number of episodes of fast but small velocity drops in June, early August, October and December which result in a saw-tooth like shape of the curves in Fig. 7. During the interval between R4 and R5 in June 2011 the seismic network was modified and stations were replaced leading to unreliable results. The causes for the changes observed in August, October, and December remain unknown. Overall interval R5 shows a relaxation pattern (Figure S3) in agreement with the absence of volcanic and seismic activity.

8. Conclusions

The use of seismic velocity variations as an observable to monitor the volcanic processes at PdF adds alternative information to the characterization of the volcanic activity. We argue that the velocity changes are caused by stress changes in the presence of the free surface. Models for the seismic velocity in stressed poroelastic materials indicate an amplification of the stress sensitivity at low lithostatic pressure close to the surface (Shapiro, 2003).

We observe a long term trend of increasing velocity that corresponds to the long term relaxation following the major crater collapse that occurred in 2007 (Peltier et al., 2010). Velocity changes related to volcanic activity are localized in the summit area with similar spatial distribution but opposite polarity for episodes of inflation and deflation indicating a common location of the pressure change. As eruptions in the post-2007 period involved only small magma volumes and short dyke propagation only within the terminal cone, deformation was also confined to the summit.

Surface displacements indicate that episodes of inflation are related to decreasing velocities and deflation corresponds to increasing velocities. Pressure changes in a magma reservoir at sea level, as indicated in various studies, would be suitable to explain the observed variations of velocities in a poro-elastic medium in the presence of the free surface. Additional to the deformation related velocity changes we observe two intervals (I1 and I4) that show decreasing velocity without detectable surface displacements prior to the occurrence of seismic crisis associated with non-eruptive dyke intrusions (I2: confirmed by GPS; I5: postulated here and indicated by slight GPS signals). We hypothesize that most of the velocity decrease in these intervals is caused by a purely elastic pressure increase in the reservoir that does not trigger seismicity. This would document a sensitivity of velocity variations to subsurface deformation that is superior to the GPS capabilities at the surface. An alternative explanation is that the velocity decrease prior to detectable deformation is caused by magmatic fluids released from the reservoir, that change the velocity of the material without notable deformation.

As every dyke intrusion originating from the reservoir is preceded by a pressurization and most likely by a release of fluids from the reservoir we conclude that a velocity decrease in the summit area without associated seismicity can indicate a forthcoming dyke intrusion. The intrusion itself causes the typical inflation signal. Whether the dyke intrusion leads to an eruption or not cannot be deduced from the pattern of the velocity changes.

Acknowledgments

This work was funded by the German Federal Ministry of Education and Research under grant FKZ:03G0736A. Data for this study was provided by the UnderVolc project supported by Agence Nationale de la Recherche under contract ANR-08-RISK-011. We greatly appreciate the comments of two anonymous reviewers.

Appendix A. Supplementary data

Supplementary data to this article can be found online at http://dx.doi.org/10.1016/j.jvolgeores.2014.02.012.

References

Aoki, Y., Takeo, M., Aoyama, H., Fujimatsu, J., Matsumoto, S., Miyamachi, H., Nakamichi, H., Ohkura, T., Ohminato, T., Oikawa, J., Tanada, R., Tsutsui, T., Yamamoto, K., Yamamoto, M., Yamasato, H., Yamawaki, T., 2009. P-wave velocity structure beneath Asama Volcano, Japan, inferred from active source seismic experiment. J. Volcanol. Geotherm. Res. 187, 272–277. http://dx.doi.org/10.1016/j.jvolgeores.2009.09.004 (URL: http://linkinghub.elsevier.com/retrieve/pii/S0377027309003564).

Battaglia, J., Ferrazzini, V., Staudacher, T., Aki, K., Cheminée, J.L., 2005. Pre-eruptive migration of earthquakes at the Piton de la Fournaise volcano (Réunion Island). Geophys. J. Int. 161, 549–558. http://dx.doi.org/10.1111/j.1365-246X.2005.02606.x.

Bensen, G.D., Ritzwoller, M.H., Barmin, M.P., Levshin, a.L., Lin, F., Moschetti, M.P., Shapiro, N.M., Yang, Y., 2007. Processing seismic ambient noise data to obtain reliable broad-band surface wave dispersion measurements. Geophys. J. Int. 169, 1239–1260. http://dx.doi.org/10.1111/j.1365-246X.2007.03374.x.

Berger, P., Got, J.L., González, C.V., Monteiller, V., 2011. Seismic tomography at Popocatépetl volcano, Mexico. J. Volcanol. Geotherm. Res. 200, 234–244. http://dx.doi.org/10.1016/j.jvolgeores.2010.12.016 (URL: http://linkinghub.elsevier.com/retrieve/pii/S0377027311000035).

Brenguier, F., Shapiro, N.M., Campillo, M., Nercessian, A., Ferrazzini, V., 2007. 3-D surface wave tomography of the Piton de la Fournaise volcano using seismic noise correlations. Geophys. Res. Lett. 34, L02305. http://dx.doi.org/10.1029/2006GL028586 (URL: http://www.agu.org/pubs/crossref/2007/2006GL028586.shtml).

Brenguier, F., Campillo, M., Hadziioannou, C., Shapiro, N.M., Nadeau, R.M., Larose, E., 2008a. Postseismic relaxation along the San Andreas fault at Parkfield from continuous seismological observations. Science (New York, N.Y.) 321, 1478–1481. http://dx.doi.org/10.1126/science.1160943 (URL: http://www.ncbi.nlm.nih.gov/pubmed/18787165).

Brenguier, F., Shapiro, N.M., Campillo, M., Ferrazzini, V., Duputel, Z., Coutant, O., Nercessian, A., 2008b. Towards forecasting volcanic eruptions using seismic noise. Nat. Geosci. 1, 126–130. http://dx.doi.org/10.1038/ngeo104.

Brenguier, F., Clarke, D., Aoki, Y., Shapiro, N.M., Campillo, M., Ferrazzini, V., 2011. Monitoring volcanoes using seismic noise correlations. Compt. Rendus Geosci. 343, 633–638. http://dx.doi.org/10.1016/j.crte.2010.12.010 (URL: http://linkinghub.elsevier.com/retrieve/pii/S1631071311000332).

Brenguier, F., Kowalski, P., Staudacher, T., Ferrazzini, V., Lauret, F., Boissier, P., Catherine, P., Lemarchand, a., Pequegnat, C., Meric, O., Pardo, C., Peltier, a., Tait, S., Shapiro, N.M., Campillo, M., Di Muro, a., 2012. First results from the UnderVolc high resolution seismic and GPS network deployed on Piton de la Fournaise volcano. Seismol. Res. Lett. 83, 97–102. http://dx.doi.org/10.1785/gssrl.83.1.97.

Calò, M., Dorbath, C., Cornet, F., Cuenot, N., 2011. Large-scale aseismic motion identified through 4-D P-wave tomography. Geophys. J. Int. 186, 1295–1314. http://dx.doi.org/10.1111/j.1365-246X.2011.05108.x.

Chen, J.H., Froment, B., Liu, Q.Y., Campillo, M., 2010. Distribution of seismic wave speed changes associated with the 12 May 2008 Mw 7.9 Wenchuan earthquake. Geophys. Res. Lett. 37. http://dx.doi.org/10.1029/2010GL044582 (n/a–n/a).

Clarke, D., Brenguier, F., Froger, J.L., Shapiro, N.M., Peltier, a., Staudacher, T., 2013. Timing of a large volcanic flank movement at Piton de la Fournaise Volcano using noise-based seismic monitoring and ground deformation measurements. Geophys. J. Int. 195, 1132–1140. http://dx.doi.org/10.1093/gji/ggt276.

Curtis, A., Gerstoft, P., Sato, H., Snieder, R., Wapenaar, K., 2006. Seismic interferometry—turning noise into signal. Lead. Edge 25, 1082. http://dx.doi.org/10.1190/1.2349814 (URL: http://link.aip.org/link/LEEDFF/v25/i9/p1082/s1&Agg=doi).

Dawson, P., Chouet, B., Okubo, P., Villaseñ[illegible]or, A., Benz, H., 1999. Three-dimensional velocity structure of the Kilauea Caldera, Hawaii. Geophys. Res. Lett. 26, 2805–2808.

Duputel, Z., Ferrazzini, V., Brenguier, F., Shapiro, N., Campillo, M., Nercessian, A., 2009. Real time monitoring of relative velocity changes using ambient seismic noise at the Piton de la Fournaise volcano (La Réunion) from January 2006 to June 2007. J. Volcanol. Geotherm. Res. 184, 164–173. http://dx.doi.org/10.1016/j.jvolgeores.2008.11.024 (URL: http://linkinghub.elsevier.com/retrieve/pii/S0377027308006239).

Got, J.L., Peltier, A., Staudacher, T., Kowalski, P., Boissier, P., 2013. Edifice strength and magma transfer modulation at Piton de la Fournaise volcano. J. Geophys. Res. Solid Earth 118. http://dx.doi.org/10.1002/jgrb.50350 (n/a–n/a).

Hadziioannou, C., Larose, E., Coutant, O., 2009. Stability of monitoring weak changes in multiply scattering media with ambient noise correlation: laboratory experiments. J. Acoust. Soc. Am. 125, 3688 (URL: http://link.aip.org/link/?JASMAN/125/3688/1).

Hobiger, M., Wegler, U., Shiomi, K., Nakahara, H., 2012. Coseismic and postseismic elastic wave velocity variations caused by the 2008 Iwate–Miyagi Nairiku earthquake, Japan. J. Geophys. Res. 117, 1–19. http://dx.doi.org/10.1029/2012JB009402 URL: http://www.agu.org/pubs/crossref/2012/2012JB009402.shtml.

Huffman, G., Adler, R., Morrissey, M., Bolvin, D., Curtis, S., Joyce, R., McGavock, B., Susskind, J., 2001. Global precipitation at one-degree daily resolution from multisatellite observations. J. Hydrometeorol. 2, 36–50 (URL: http://journals.ametsoc.org/doi/abs/10.1175/1525-7541(2001)002%3C0036:GPAODD%3E2.0.CO%3B2).

Larose, E., Margerin, L., Derode, A., van Tiggelen, B., Campillo, M., Shapiro, N., Paul, A., Stehly, L., Tanter, M., 2006. Correlation of random wavefields: an interdisciplinary review. Geophysics 71, SI11–SI21. http://dx.doi.org/10.1190/1.2213356.

Larose, E., Planes, T., Rossetto, V., Margerin, L., 2010. Locating a small change in a multiple scattering environment. Appl. Phys. Lett. 96, 204101. http://dx.doi.org/10.1063/1.3431269 (URL: http://link.aip.org/link/APPLAB/v96/i20/p204101/s1&Agg=doi).

Massin, F., Ferrazzini, V., Bachèlery, P., Nercessian, A., Duputel, Z., Staudacher, T., 2011. Structures and evolution of the plumbing system of Piton de la Fournaise volcano inferred from clustering of 2007 eruptive cycle seismicity. J. Volcanol. Geotherm. Res. 202, 96–106. http://dx.doi.org/10.1016/j.jvolgeores.2011.01.008 (URL: http://linkinghub.elsevier.com/retrieve/pii/S0377027311000333).

Meier, U., Shapiro, N.M., Brenguier, F., 2010. Detecting seasonal variations in seismic velocities within Los Angeles basin from correlations of ambient seismic noise. Geophys. J. Int. 985–996. http://dx.doi.org/10.1111/j.1365-246X.2010.04550.x.

Mordret, A., Jolly, A., Duputel, Z., Fournier, N., 2010. Monitoring of phreatic eruptions using Interferometry on Retrieved Cross-Correlation Function from Ambient Seismic Noise: results from Mt. Ruapehu, New Zealand. J. Volcanol. Geotherm. Res. 191, 46–59. http://dx.doi.org/10.1016/j.jvolgeores.2010.01.010 URL: http://linkinghub.elsevier.com/retrieve/pii/S0377027310000247.

Nagaoka, Y., Nishida, K., Aoki, Y., Takeo, M., Ohminato, T., 2012. Seismic imaging of magma chamber beneath an active volcano. Earth Planet. Sci. Lett. 333–334, 1–8. http://dx.doi.org/10.1016/j.epsl.2012.03.034 (URL: http://linkinghub.elsevier.com/retrieve/pii/S0012821X1200163X).

Obermann, A., Planes, T., Larose, E., Sens-Schönfelder, C., Campillo, M., 2013. Depth sensitivity of seismic coda waves to velocity perturbations in an elastic heterogeneous medium. Geophys. J. Int.. http://dx.doi.org/10.1093/gji/ggt043.

Pacheco, C., Snieder, R., 2005. Time-lapse travel time change of multiply scattered acoustic waves. J. Acoust. Soc. Am. 118, 1300. http://dx.doi.org/10.1121/1.2000827 (URL: http://link.aip.org/link/JASMAN/v118/i3/p1300/s1&Agg=doi).

Pacheco, C., Snieder, R., 2006. Time-lapse traveltime change of singly scattered acoustic waves. Geophys. J. Int. 165, 485–500. http://dx.doi.org/10.1111/j.1365-246X.2006.02856.x.

Patanè, D., Barberi, G., Cocina, O., De Gori, P., Chiarabba, C., 2006. Time-resolved seismic tomography detects magma intrusions at Mount Etna. Science (New York, N.Y.) 313, 821–823. http://dx.doi.org/10.1126/science.1127724 (URL: http://www.ncbi.nlm.nih.gov/pubmed/16902133).

Peltier, A., Bachèlery, P., Staudacher, T., 2009. Magma transport and storage at Piton de La Fournaise (La Réunion) between 1972 and 2007: a review of geophysical and geochemical data. J. Volcanol. Geotherm. Res. 184, 93–108. http://dx.doi.org/10.1016/j.jvolgeores.2008.12.008 (URL: http://linkinghub.elsevier.com/retrieve/pii/S0377027308006550).

Peltier, A., Staudacher, T., Bachèlery, P., 2010. New behaviour of the Piton de La Fournaise volcano feeding system (La Réunion Island) deduced from GPS data: influence of the 2007 Dolomieu caldera collapse. J. Volcanol. Geotherm. Res. 192, 48–56. http://dx.doi.org/10.1016/j.jvolgeores.2010.02.007 (URL: http://linkinghub.elsevier.com/retrieve/pii/S037702731000051X).

Planès, T., Larose, E., Margerin, L., Rossetto, V., Sens-Schönfelder, C., 2014. Decorrelation and phase-shift of coda waves induced by local changes: multiple scattering approach and numerical validation. Waves in Random and Complex Media. Taylor & Francis, pp. 1–27. http://dx.doi.org/10.1080/17455030.2014.880821.

Poupinet, G., Ellsworth, W., Frechet, J., 1984. Monitoring velocity variations in the crust using earthquake doublets: an application to the Calaveras Fault, California. J. Geophys. Res. 89, 5719–5731 (URL: http://digitalcommons.unl.edu/usgsstaffpub/386/).

Richter, T., Sens-Schönfelder, C., Asch, G., Kind, R., 2014. Comprehensive observation and modeling of earthquake and temperature related seismic velocity changes in northern Chile with passive image interferometry. J. Geophys. Res. (submitted for publication).

Rossetto, V., Margerin, L., Planes, T., Larose, E., 2011. Locating a weak change using diffuse waves: theoretical approach and inversion procedure. J. Appl. Phys. 109, 034903. http://dx.doi.org/10.1063/1.3544503 (URL: http://link.aip.org/link/JAPIAU/v109/i3/p034903/s1&Agg=doi).

Roult, G., Peltier, A., Taisne, B., Staudacher, T., Ferrazzini, V., Di Muro, A., 2012. A new comprehensive classification of the Piton de la Fournaise activity spanning the 1985–2010 period. Search and analysis of short-term precursors from a broad-band seismological station. J. Volcanol. Geotherm. Res. 241–242, 78–104. http://dx.doi.org/10.1016/j.jvolgeores.2012.06.012 URL: http://linkinghub.elsevier.com/retrieve/pii/S0377027312001801.

Sens-Schönfelder, C., 2008. Synchronizing seismic networks with ambient noise. Geophys. J. Int. 174, 966–970. http://dx.doi.org/10.1111/j.1365-246X.2008.03842.x.

Sens-Schönfelder, C., Larose, E., 2008. Temporal changes in the lunar soil from correlation of diffuse vibrations. Phys. Rev. E. 78, 1–4. http://dx.doi.org/10.1103/PhysRevE.78.045601.

Sens-Schönfelder, C., Wegler, U., 2006. Passive image interferometry and seasonal variations of seismic velocities at Merapi Volcano, Indonesia. Geophys. Res. Lett. 33, 1–5. http://dx.doi.org/10.1029/2006GL027797 (URL: http://www.agu.org/pubs/crossref/2006/2006GL027797.shtml).

Sens-Schönfelder, C., Wegler, U., 2011. Passive image interferometry for monitoring crustal changes with ambient seismic noise. Compt. Rendus Geosci. 343, 639–651. http://dx.doi.org/10.1016/j.crte.2011.02.005 (URL: http://linkinghub.elsevier.com/retrieve/pii/S1631071311000861).

Shapiro, S., 2003. Elastic piezosensitivity of porous and fractured rocks. Geophysics 68, 482–486. http://dx.doi.org/10.1190/1.1567215.

Snieder, R., 2006. The theory of coda wave interferometry. Pure Appl. Geophys. 163, 455–473. http://dx.doi.org/10.1007/s00024-005-0026-6.

Snieder, R., Grêt, A., Douma, H., Scales, J., 2002. Coda wave interferometry for estimating nonlinear behavior in seismic velocity. Science (New York, N.Y.) 295, 2253–2255. http://dx.doi.org/10.1126/science.1070015 (URL: http://www.ncbi.nlm.nih.gov/pubmed/11910107).

Staudacher, T., Peltier, A., 2014. Ground deformation at Piton de la Fournaise (La Réunion Island), a review from 20 years of GNSS monitoring. Springer (submitted for publication).

Toupin, R., Bernstein, B., 1961. Sound waves in deformed perfectly elastic materials. Acoustoelastic effect. J. Acoust. Soc. Am. 33 (URL: http://asadl.org/jasa/resource/1/jasman/v33/i2/p216_s1).

Wapenaar, K., Draganov, D., Snieder, R., 2010. Tutorial on seismic interferometry: Part 1. Basic principles and applications. Geophysics 75. http://dx.doi.org/10.1190/1.3457445.

Weaver, R.L., Hadziioannou, C., Larose, E., Campillo, M., 2011. On the precision of noise correlation interferometry. Geophys. J. Int. 185, 1384–1392. http://dx.doi.org/10.1111/j.1365-246X.2011.05015.x.

Wegler, U., Nakahara, H., Sens-Schönfelder, C., Korn, M., Shiomi, K., 2009. Sudden drop of seismic velocity after the 2004 M w 6.6 mid-Niigata earthquake, Japan, observed with Passive Image Interferometry. J. Geophys. Res. 114, 1–11. http://dx.doi.org/10.1029/2008JB005869 (URL: http://www.agu.org/pubs/crossref/2009/2008JB005869.shtml).